Chiral Opto-Electronic Functionalities via DNA-Organic Semiconductor Complex

- 2 Moon Jong Han¹, Hee Seong Yun², Yongjoon Cho³, Minkyu Kim¹, Changduk Yang³, Vladimir
- 3 Tsukruk^{1,*}, and Dong Ki Yoon^{2,4,5,*}

4

1

- ¹School of Materials Science and Engineering, Georgia Institute of Technology, Atlanta, GA
- 6 30332, USA
- ²Department of Chemistry, Korea Advanced Institute of Science and Technology, Daejeon
- 8 34141, Republic of Korea
- 9 ³Department of Energy Engineering, School of Energy and Chemical Engineering,
- 10 Perovtronics Research Center, Low Dimensional Carbon Materials Center, Ulsan National
- 11 Institute of Science and Technology (UNIST), Ulsan 44919, Republic of Korea
- ⁴Graduate School of Nanoscience and Technology, Korea Advanced Institute of Science and
- 13 Technology, Daejeon 34141, Republic of Korea
- 14 ⁵KAIST Institute for Nanocentury, Korea Advanced Institute of Science and Technology,
- 15 Daejeon 34141, Republic of Korea
- *To whom correspondence should be addressed.
- 17 E-mail: vladimir@mse.gatech.edu and nandk@kaist.ac.kr

Chiral Opto-Electronic Functionalities via DNA-Organic Semiconductor Complex

3 Moon Jong Han¹, Hee Seong Yun², Yongjoon Cho³, Minkyu Kim¹, Changduk Yang³, Vladimir

4 Tsukruk^{1,*}, and Dong Ki Yoon^{2,4,5,*}

We fabricate the bio-organic field-effect transistor (BOFET) with the DNA-perylene diimide (PDI) complex, showing unusual chiroptical and electrical functionalities. DNA is used as the chirality-inducing scaffold and charge-injection layer. The shear-oriented film of the DNA-PDI complex shows how large-area periodic molecular orientation and charge transport are related, generating drastically different optoelectronic properties at each DNA/PDI concentration. Resultant BOFET reveals chiral structures with high electron mobility, photoresponsivity, and photosensitivity, reaching 3.97 cm² V⁻¹ s⁻¹, 1.18 A W⁻¹, and 7.76 × 10³, respectively. Interestingly, the BOFET enables the definitive response to the handedness of circularly polarized light. We suggest our work can be a cornerstone for the natural chirality and anisotropy of DNA material and the electron conductivity of organic semiconducting molecules to be mutually used in the unique

chiro-optoelectronic functions as added ability to traditional OFET.

For the next generation of the internet of thing (IoT) based on large-scale production and ultimate commercialization, it is required to demonstrate "green" solvent-soluble organic semiconductors for electronics like organic field-effect transistors (OFETs) and organic phototransistors (OPTs) with high-performance and multi-functionalities. It is also valuable for facilitating different prospective applications in optoelectronics, biomedical sensing, and wearable electronics¹⁻³. To date, significant progress of organic semiconductors (OSCs) based on the halogenated and aromatic hydrocarbon solvents has been achieved by molecule design^{4,5}, crystal engineering^{6,7} and film fabrication techniques⁸⁻¹². However, there are still challenging research topics in the self-assembly process, and localized aggregation of sustainable OSCs such as conjugated polymers and supramolecules during evaporation of green solvents, which is essential to control the molecular orientation and the resultant optoelectrical properties. The molecular ordering and orientation control the charge carrier mobility of OSC films and interfaces among OSC, source/drain, and the dielectric layer¹³⁻¹⁵. The solution-processed organic thin films are mainly sensitive to the fabrication conditions such as solvent-evaporation rate¹⁶ and liquid surface tension^{17,18}. Nevertheless, it remains challenging to control the evaporation of solvents and phase aggregation, which can deteriorate device performance 19,20.

1

2

3

4

5

6

7

8

9

10

11

12

13

14

15

16

17

18

19

20

21

22

23

24

Generally, it is well known that the inter-and intramolecular organization of OSCs directly governs the charge carrier transport to minimize the domain boundaries and defect generation while ensuring in-plane π - π stacking to avoid the undesired charge scattering or trapping²¹. Thus, various solution-processable methods have been suggested to induce the ordered and oriented structures²² by facilitating meniscus-guided shearing²³, off-center spin-coating⁸, mechanical rubbing methods¹¹, and the use of confined fluid flow on pre-engraved substrates^{24,25}. Especially liquid crystalline (LC) materials are considered for fabrication of long-range orientation and zigzag-like chiral morphologies with added functionalities under

controlled shearing conditions²⁶⁻³⁰, which can be critical in the scaffold to fabricate the largearea well-ordered and orient OSCs.

The host-guest co-assembly of different kinds of components can generate various intriguing molecular organizations to enhance optoelectronic functionalities³¹. Significantly, the chiral host molecule or structure can guide and modulate the ordering and orientation of guest materials in a chiral-induced manner, which are not easily obtained using traditional synthetic materials³²⁻³⁴. So, various chiral biological materials such as DNA³⁵, M13 bacteriophage³⁶, cellulose³⁷, chitin³⁸ have been studied to control the guest molecule chiral organization. The zigzag-like structures were formed from alternately oriented DNA chains with wall-defects in the lyotropic LC phase during drying DNA droplets^{39,40}. It results from the competition between the radial dilative stress near the contact line of the droplet and DNA elasticity, revealing periodic undulations as deformed zigzag patterns.^{39,40} However, this technique could only control the local DNA structures at the edge of the droplet with irregular periodicity on large scale. Therefore it was hard to get the highly ordered domains extending across macroscopic thin films critical for device performance.

Here, we report the sheared-oriented perylene diimide (PDI)-DNA complex thin film obtained by the shearing method, showing how molecular orientation and charge transport are collectively controlled near the contact line (Fig. 1a). The well-ordered and oriented supramolecular structures are formed with high electron mobility and photosensitivity by facilitating the versatility of DNA as a chiral template and charge-injection layer. The resultant organized thin film of the DNA-PDI complex can be used to fabricate bio-organic field-effect transistor (BOFET), showing the electric response to the handedness of circularly polarized light as a new added functionality. The functional convergence between the natural chirality of DNA and the electron conductivity of OSC facilitates the novel chiro-electro-optical response,

which can be widely used in nature abundant chiral biological materials.

2

3

4

5

6

7

8

9

10

11

12

13

14

15

16

17

18

19

20

1

Experimental Approaches

Commercially available DNA materials from salmon sperm and the synthesized N,N'di(propanoic acid)-perylene-3,4,9,10-tetracarboxylic diimide (PA-PTCDI) (denoted by PDI) are prepared as the host and guest materials (Fig. 1, see Methods)⁴¹. The appropriate miscibility of DNA and PDI in the water is important to achieve a homogeneous solution and guarantee the shearing-aligned films onto the substrate. The phosphate groups on the DNA chains and carboxylic groups within the PDI molecules make DNA-PDI complex dissolve in water, showing the random dispersion or the isotropic phase (Figure 1b)³⁸⁻⁴⁰. For the systematic studies of the resultant molecular orientation, DNA (0.5, 1, and 2 mg) is added to the aqueous PDI solution (10 mg/ mL; 100% in weight ratio) to make PDI (95.2 %) + DNA (4.8 %), PDI (90.9 %) + DNA (9.1 %), and PDI (83.3 %) + DNA (16.7 %) solutions. The mixed solutions are magnetically stirred at 20 °C for 12 hrs. After filtering through a syringe filter, the solution is placed between two glass substrates, where the top substrate is treated with tridecafluoro-1,1,2,2,-tetrahydrooctyltrichlorosilane (FOTS) self-assembled monolayer (Fig. 1b). DNA-PDI thin films are fabricated by the solution shearing process, as reported before (Fig. 1a)¹⁶. The pulling speed of the top substrate is fixed at 30 µm/s to control the molecular orientation during solvent evaporation, generating zigzag-like structures depending on DNA concentration (Figure 1c).

21

22

Periodic Molecular Orientation by Shearing Coating

The different molecular orientations by solution shearing depending on DNA concentration are directly observed by polarized optical microscopy (POM) and atomic force microscopy (AFM) (Fig. 2). The meniscus-guided self-assembly of the DNA-PDI complex at the air-liquid-solid triplet contact line generates variously oriented microfibrils^{29,42}. For pristine PDI film (Fig. 2a), the resultant local domains with random orientation to the shearing direction (red arrows in Fig. 2) are visualized by POM and AFM measurements due to the less ordered PDIs. Note that the PDI molecules are not well ordered without DNA template or nonsolvent⁴¹, which is confirmed by the weak linear dichroism of the PDI film under a single linear polarizer. The sheared neat PDI film reveals no change in transmittance upon sample rotation; POM results presented an almost dark image regardless of the rotation angle, confirming this, although some oriented tendency can be observed in the AFM micrograph.

On the contrary, the sheared films of the DNA-PDI mixed solutions exhibit clear linear dichroism (Figure 2b–d). The transition dipole moment along the long axis of the conjugated small molecule is perpendicular to the shearing direction. These results strongly suggest that the DNA template enhances the ordering of PDI aggregates into the oriented microfibrils that have good interconnectivity between domains (Figure 2b–d). To confirm the orientation of the DNA-PDI aggregates, the first-order retardation plate ($\lambda = 530$ nm) is inserted between the sample and the analyzer. Color changes are observed due to the retardation of the light after passing each sample and the retardation plate. When the optic axis of the positive birefringent materials is parallel to the two crossed polarizers, a magenta color appears. Cyan or yellow color appears when the optic axis is parallel or perpendicular to the slow axis of the retardation plate, respectively. DNA and PDI molecules stack perpendicular to the long axis of the columnar aggregates, indicating negative birefringence, which results in the opposite trend of color changes with the retardation plate, e.g., yellow to cyan and cyan to yellow at each

condition²⁸. From the POM measurement, we hypothesize that the DNA molecules aligned parallel to the shearing direction by confirming the yellowish or blueish color appearance by rotating samples with crossed polarizers and the retardation plate^{29,30}.

More evidence for DNA-templated PDI aggregates emerged in the solution-sheared films is demonstrated by the angular distribution map derived from the corresponding AFM height images using GTFiber.⁴³ By comparing the average director from the angular distribution for each film condition at a constant shearing speed, it is determined that the DNA-PDI aggregates are oriented perpendicular to the shearing direction as the DNA concentration increases, in which the overall molecular orientation order parameter is 0.43, 0.07, 0.55, and 0.80 (see Methods) for PDI (100 %), PDI + DNA (95.2: 4.8 %), PDI + DNA (90.9: 9.1 %), and PDI + DNA (83.3: 16.7 %), respectively. 0.43 for PDI (100 %) looks weird to show an even higher value compared to PDI + DNA (95.2: 4.8 %)'s 0.007. Still, AFM topographic image itself shows irregular textures, and the order parameter (*S*) based on the UV-vis spectroscopy reveals the optically-related orientation at large-scale (Fig. S1).⁴⁴

15
$$S = (A_{\parallel} - A_{\perp})/(A_{\parallel} + 2A_{\perp})$$

 A_{\parallel} and A_{\perp} correspond to the light absorption parallel or perpendicular to the long axis of the 17 conjugated PDI molecule, respectively. *S* of each concentration condition is 0.0033, 0.085, 0.28, 18 and 0.46 for PDI (100 %), PDI + DNA (95.2: 4.8 %), PDI + DNA (90.9: 9.1 %), and PDI + 19 DNA (83.3: 16.7 %), respectively.

Specifically, the zigzag-like structures result from DNA molecules exhibit two or one axes to the horizontal axis with deviation angle depending on the degree of dilative stress (Fig. 2b-d). The two axes exist in angle between 48.5° and 131° for PDI (95.2 %) + DNA (4.8 %), 30° and 150° PDI (90.9 %) + DNA (9.1 %). Their deviation angles are varied from 18° to 21°

and from 15° to 16°, respectively. For PDI (83.3 %) + DNA (16.7 %), the deviation angles are ~ 30° to the horizontal axis, exhibiting deformed zigzag-like conformation.

In order to understand the origin of periodic patterns generated in Fig. 2, changes in the orientation of DNA-PDI complexes are investigated by POM using a retardation plate following the evaporation process with magnified images (Fig. S2 and S3). It was reported that the DNA droplet sample showed randomly oriented small yellow and blue domains, regardless of the evaporation of water without the shearing process⁴⁰. On the other hand, a mechanically sheared DNA-PDI film reveals the generation of wavy structures as the water evaporates. During the evaporation of water, the contact angle (σ) of a contact line decreases gradually to induce depinning and receding the CL when σ reaches at 2°-4°³⁷. The retraction of the CL and an increase of local density of the DNA-PDI complex in the more condensed state induces dilative stress near the CL, which can be relaxed to form the undulated DNA-PDI⁴⁵. The deformation of the DNA-PDI complex is described by considering elastic free energy of DNA chains^{37,46},

$$f = \frac{K_1}{2} (\nabla \cdot \vec{n})^2 + \frac{K_2}{2} (\vec{n} \cdot (\nabla \times \vec{n}))^2 + \frac{K_3}{2} (\vec{n} \times (\nabla \times \vec{n}))^2 + \frac{E}{2} \frac{\partial \rho_p}{\partial \rho_p^0}$$

The first three terms are the Frank elastic terms, in which K_1 , K_2 , and K_3 are elastic constants for splay, twist, and bend deformations, respectively. The last term is a free energy cost for the locally dilated DNA chains, where $\partial \rho_p$ is a variation of the local DNA density, ρ_p^0 is the average DNA density, and E is elastic compressibility induced by dilative stress.

It is well-known that the DNA chain is regarded as a semi-flexible chain in terms of elastic behavior, where the splay deformation hardly occurs because there are fewer free-ends available to fill the splay-induced gaps, resulting in $K_1 >> K_2$, K_3^{47} . The twist term, K_2 , is also

suppressed with increasing the DNA contour length³⁷. Therefore, the gained energy from the 1 2

last term by receding CL should be relaxed by bend deformation, resulting in periodic twisted

hierarchical structures at PDI (90.9 %) + DNA (9.1 %) condition.

As the concentration of DNA increases at a fixed concentration of PDI, a more condensed DNA-PDI complex is compressed and accumulated near the contact line, which is in line with the common phenomena of the high thickness of deposited films⁴⁸. Therefore, the degree of compression/accumulation increases for PDI (83.3 %) + DNA (16.7 %) condition, but the hydrodynamic effect decreases compared to the PDI (90.9 %) + DNA (9.1 %), exhibiting the distinct perpendicular orientation of average aggregates axis to the shearing direction as shown in Fig. 2. As increasing the pulling velocity ($v = 150 \mu m/s$) in the solution shearing process (Fig. S4), the hydrodynamic effect is relatively dominant during solvent evaporation as internal flow increases The average axis of aggregates is parallel to the shearing direction³⁰.

14

15

16

17

18

19

20

21

22

23

3

4

5

6

7

8

9

10

11

12

13

Chiro-Optical Behavior of DNA-PDI Complex Supramolecular Structures

The optical properties of PDI and DNA-PDI complex in deionized (DI) water $(1.0 \times 10^{-4} \text{ M})$ are measured by UV-vis spectroscopy to show a characteristic dimeric peak at 500 nm and a shoulder close to 544 nm (Fig. 3a). The relative intensity between the vibronic $0 \rightarrow 1$ band in the $\pi \to \pi^*$ electronic transition (A₀₋₀/A₀₋₁ < 0.6) is the reversal of that of monomeric PDI (for which $A_{0-0}/A_{0-1} > 1$). Generally, PDIs self-organize into one-dimensional (1D) aggregates upon adjustment of solution pH. The introduction of DNA (2 mg/ mL) to PDI is negligible on pH as shown in the optical properties.

The solution-sheared films are prepared on the quartz to investigate the absorption

spectra in PDI and DNA-PDI complex in the film (Fig. 3b). Compared to the absorption spectra of solutions, there is a blue shift in the film's state and a Frank-Condon ratio A₀₋₁/A₀₋₀ greater than one is indicative of the strong and effective H-aggregation via cofacial π– π stacking between the PDI cores. Additionally, the films exhibit two new bands at 515 nm and 580 nm by increasing DNA concentration, implying anion- π interactions between the phosphates

group in DNA molecules and electron-deficient PDI core⁴⁹.

Circular dichroism (CD) spectra are measured to investigate solution-shearing effects on the chirality of DNA-PDI aggregates in both their monomeric and aggregated states. No CD signals are observed above 300 nm using a solution of DNA, PDI, and DNA-PDI complex in DI water at a 10⁻⁴ M (Fig. 3c). It indicates that chirality is not transferred from the molecular chirality of DNA to the PDI core in the solution state. The solution-sheared DNA-PDI aggregates exhibit strong CD peaks between 300 and 700 nm, displaying the cooperative aggregation phenomenon-induced CD effect^{50,51}. This indicates successful chiral inducement and amplification from the molecular chirality of DNA to the nonchiral PDI molecules forming DNA-PDI complex aggregates. The CD spectrum of DNA-PDI aggregates contains one main negative peak at 450 nm, exhibiting a bisignated Cotton effect with a positive peak at 575 nm and 590 nm as DNA concentration increases (Fig. 3d).

In the monomeric state, chirality originates from intramolecular interactions. After self-assembling process, both intra- and intermolecular interactions contribute to the supramolecular chirality of aggregates, which amplifies the intensity of the CD peaks⁵². By comparing the relative chirality of pristine PDI and DNA-PDI aggregates, we can conclude that solution shearing greatly induces on the supramolecular chirality²⁵.

Chiro-Electrical Properties of DNA-PDI Complex-based BOFETs

- 2 To investigate the charge transport characteristics of solution sheared DNA-PDI film, bottom-
- 3 gate top-contact (BGTC) BOFETs are fabricated on SiO₂-coated n-doped Si substrates, whose
- 4 channel width and length are 500 μm and 50 μm, respectively. (Fig. 4, see Methods) The gold
- source/drain electrodes are thermally deposited perpendicular (\perp) and parallel (\parallel) to the
- 6 shearing direction (Fig. 4a).

1

7

8

9

10

11

12

13

14

15

16

17

18

19

20

21

22

23

24

The representative transfer curves (Fig. 4b,c) are characterized for films based on the various solutions condition, including PDI (100 %), PDI + DNA (95.2 : 4.8 %), PDI + DNA (90.9:9.1%), and PDI + DNA (83.3:16.7%). The charge carrier mobility, I_{ON}/I_{OFF} , and threshold voltage (V_{th}) are calculated in the saturation region of the transfer curves (Table 1). Neat PDI film in Figure 3a exhibits low charge carrier mobility of $\sim 3.0 \times 10^{-3}$ cm² V⁻¹ s⁻¹ and the negligible difference in drain current for devices fabricated by shearing in the perpendicular and parallel directions because of the less oriented PDI aggregates as discussed above (Fig. S1). For the highly ordered and aligned DNA-PDI complex films, such as those obtained from the PDI + DNA (83.3: 16.7 %) solution, the charge carrier mobility is relatively high and exhibits distinctly different average values of 3.97 cm 2 V $^{-1}$ s $^{-1}$ and 0.16 cm 2 V $^{-1}$ s $^{-1}$ with perpendicular and parallel shearing directions, respectively. The highly oriented aggregates for the PDI + DNA (90.9: 9.1 %) condition exhibits higher electrical anisotropy than the PDI + DNA (90.9: 9.1 %) case, which coincides with anisotropic optical properties extracted from the dichroism and order parameters from POM and AFM images (Fig. 2 and Fig. S1). These systematic results can support that the intermolecular charge transport of highly aligned nanofibrillar structures oriented parallel with source/drain channel direction is more effective than when their orientation is perpendicular to the channel direction. Note that intermolecular charge transport via π - π stacking between the conjugated small molecule is faster than intramolecular

- 1 charge transport along the long axis direction of the conjugated small molecule^{53,54}. The
- 2 representative output curves are measured for the films of the pristine PDI (100 %) and PDI +
- 3 DNA (83.3: 16.7 %) condition as well (Fig. 4d,e).

- To further investigate the performance of sheared DNA-PDI complex films, contact resistance (R_CW) associated with the DNA-PDI aggregates/Au interface is analyzed by the transmission line method (TLM) (Fig. S5). The total channel resistance ($R_{ON}W$) is extracted from the linear regime of the output curves at V_{GS} = + 80 V. The R_CW results from the intercept of the line fits for each channel length (50, 100, 150, 200 µm) are reduced from 4.195 M Ω cm for neat PDI (100 %) film to 0.125 M Ω cm for PDI + DNA (83.3: 16.7 %) film. The improved charge carrier mobility derived from the decreased contact resistance measured in PDI + DNA (83.3: 16.7 %) film suggests that DNA chains may serve as a charge injection layer at the electrode/organic semiconductor interface, though the mechanism requires further elucidation 55,56. Conceivably, the interfacial dipoles induced by the phosphate groups present on the DNA material facilitate charge injection at the electrode/organic semiconductor interface, reducing the charge injection barrier.
 - The CD signal is detected at the 465 nm wavelength range in PDI + DNA (83.3: 16.7 %), which is comparable with the pristine PDI (100 %) condition. It corresponds to the improvement of electrical properties under LEDs with electroluminescence emission peaks at 465 nm (1 mW cm⁻² intensity) for the PDI + DNA (83.3: 16.7 %) film, compared to the PDI (100 %) film due to the effect of aggregates formation. Fig. 5a shows the transfer characteristics of the sheared films under illumination with the gate voltage sweeping from -20 V to 80 V and a fixed drain voltage of 80 V, respectively. For the DNA-PDI film, the apparent increase of I_{DS} and negative shift of V_{th} , relative to the measured under dark conditions, is related to photogenerated carriers compared to the pristine PDI film case.

The DNA-PDI films exhibit larger domains than the pristine PDI film (Fig.2), leading to the faster charge carrier transport and exciton dissociation/separation upon the light exposure. The significant enhancement in photocurrent and the V_{th} shifts can be attributed to the generation of photoexcited charge carriers and elimination of trap sites, leading to easier exciton dissociation, exciton separation, and charge transport⁵⁷⁻⁵⁹.

Photoresponsivity (R) and photosensitivity (P) are critical factors used to evaluate the performance of OPTs can be determined from their transfer characteristics (see Methods).REF Phototransistors can utilize the gate effect to modulate R and P for practical applications. The R and P values are calculated for the pristine PDI and DNA-PDI aggregates-based OPTs under a light intensity of 1 mW cm⁻² (Fig. 5b). DNA-PDI complex films show good optical performance with maximum P and R values of 7.66×10^3 and 1.18 A W^{-1} . In contrast, the pristine DNA-PDI films exhibit maximum P and R values of only 1.13×10^1 and $2.39 \times 10^{-4} \text{ A W}^{-1}$, respectively. It might be explained by a relatively large interfacial area, and more intensive interfacial charge trapping of DNA-PDI aggregates condition than that of the pristine PDI film. The poor phototransistor performance of PDI films results from inefficient charge transport because of the lack of π - π stacking. The maximum P of PDI/ DNA aggregates-based OPTs is obtained at $V_G = 0$ V because the output current of an illuminated OPT (I_{light}) consists of the field-effect-induced current (I_{field}) and photocurrent whereas the output current in the dark (I_{dark}) consists of I_{field} only. When the transistor is turned off, I_{field} is very low, so the ratio I_{light}/I_{dark} is high.

When the BOFET is turned on by applying a higher positive V_G , I_{field} can increase significantly, leading to an increased dark current and a decreased I_{light}/I_{dark} . Additionally, we examine the chiro-electrical response of the pristine PDI and DNA-PDI complex-based OPTs by manipulating the circularly polarized light (CPL) as schematically illustrated in the Fig. 5c.

Under irradiation of CPL (λ = 460 nm, 1 mW cm⁻²) with different polarizations such as right-handed CPL (RCPL) and left-handed CPL (LCPL), the distinct real-time photocurrent signals are recorded in V_G = 80 V and V_{DS} = 80 V (Fig. 5d). The DNA-PDI complex-based OPTs exhibit higher photocurrent under the RCPL illumination matching very well with the results of CD spectra, originated from the induced zigzag-like supramolecular organization. At the same time, the pristine PDI-based OFETs do not respond to the CPL due to nonchiral structure and the resultant no CD spectral sensitivity.

8

9

10

11

12

13

14

15

16

17

18

19

20

21

22

23

Conclusion

In this work, we successfully explore the systematic study of the ordering and orientation of semiconducting molecules by facilitating the DNA scaffold and evaporation-induced selfassembly process. Different periodic zigzag-like chiral structures are demonstrated by varying **DNA** concentration and pulling speed in the system. Dilative stress and compression/accumulation phenomena near the CL during solvent evaporation enable to orient the DNA/OSC complex, showing the unique chiroptical functionality, in which DNA chains act as a scaffold and charge injection layer. In particular, the highly ordered and oriented chiral structures of DNA-templated OSC exhibits electron mobility as high as 3.97 cm² V⁻¹ s⁻¹ and maximum P, R values of 7.66 \times 10³ and 1.18 A W⁻¹, respectively, which is 3 orders of magnitude higher compared to the condition of pristine PDI. Moreover, BOSET possess the unique ability to provide added selective detection of CPL to facilitate additional functionality and control. The pioneering approach presented here will provide opportunities for the natureabundant chiral biomaterials in chiroptical and optoelectronic applications for enhanced thin film bio-electronical devices.

Acknowledgements

- 2 Financial support for this research was provided by the NSF-CBET grant 180349, Air Force
- 3 Research Laboratory grant FA8650-D-16-5404, and Air Force Office for Scientific Research
- 4 grant FA9550-20-1-0305. This work was also supported by a grant from the National Research
- 5 Foundation (NRF) (MSIT: 2017R1E1A1A01072798, 2018R1A5A1025208,
- 6 2021M3H4A3A01050378, and 2021R1A6A3A14039290.)

7

8

1

Author contributions

- 9 M.J.H. and D.K.Y. designed the research; M.J.H. and H. S. Y. performed experimental works and
- 10 Y. C., and C. Y. synthesized N,N'-di(propanoic acid)-perylene-3,4,9,10-tetracarboxylic diimide
- 11 (PA-PTCDI) molecules; M. K. conducted CD measurement; M.J.H., V. T., and D.K.Y. analyzed
- 12 results and wrote the manuscript.

13

14

Additional information

- 15 Reprints and permissions information is available at www.nature.com/naturecommunications. The
- authors declare no competing financial interests. Readers are welcome to comment on the online
- 17 version of this article at www.nature.com/nature. Correspondence and requests for materials should
- be addressed to V. T. (vladimir@mse.gatech.edu) and D.K.Y. (nandk@kaist.ac.kr).

19

20

Methods

- 1 Materials and Solution Processing: Water-soluble N,N'-di(propanoic acid)-perylene-3,4,9,10-
- 2 tetracarboxylic diimide (PA-PTCDI) was synthesized following the literature method. 41 It was
- 3 dissolved in deionized water at 10 mg/ mL with further stirring for 12 h at 60 °C. Then, each
- 4 weights (1.5, 3, 7.5 mg) of DNA (deoxylibonucleic acid sodium salt from salmon tests, Sigma-
- 5 Aldrich) was dissolved in the PA-PTCDI solutions, resulting in PA-PTCDI (10 mg/ mL) +
- 6 DNA (0.5 mg/mL), PA-PTCDI (10 mg/mL) + DNA (1 mg/mL), and PA-PTCDI (10 mg/mL)
- 7 + DNA (2 mg/ mL) solutions for about 10 h, which were filtered through a 0.2 μm syringe filter
- 8 of $0.2 \mu m$ pore size.
- 9 Fabrication and optoelectronic measurement of BOFET: The bottom-gate top-contact configuration of OFETs was fabricated on a heavily n-doped silicon wafer, in which a thermally 10 grown 300 nm thick SiO₂ acted as the gate dielectric layer. The substrates were cleaned 11 following sequential rinsing with acetone, ethanol, and deionized water for 15 min each in an 12 ultrasound cleaning bath. The OSC layers were shear-coated onto the precleaned substrates 13 14 with 30 μm/s pulling speed, where the top slide glass was treated with tridecafluoro-1,1,2,2,tetrahydrooctyltrichlorosilane (FOTS) self-assembled monolayer. All the experiments were 15 performed at 40 °C. The Au source and drain electrodes (50 nm) was thermally evaporated 16 17 using a shadow mask. The current-voltage characteristics of the OFETs were measured within a N₂-filled glove box, by using a Keithley 4200A-SCS semiconductor parameter analyzer. The 18 charge carrier mobility (µ) was calculated by using the following equation from the saturated 19 region in the transfer curve, 20

21
$$I_{DS} = (WC_i/2L)\mu(V_{GS} - V_{th})^2$$

- where W and L refer to the channel width (50 μ m) and length (500 μ m), respectively. C_i is the
- areal capacitance of the SiO₂ gate dielectric (1.04 × 10^{-8} F cm⁻²), and V_{th} is threshold voltage.

- 1 V_{th} was extracted via a linear fitting of $-I_{DS}$ versus V_G , which is based on the linear transfer
- 2 data.
- 3 Optoelectronic characterization was conducted by measuring the current-voltage
- 4 characteristics of the fabricated devices in the dark environment and under illumination
- 5 intensity (1 mW cm⁻²) using light-emitting diodes (LEDs) (Thorlab). Specifically, LEDs with
- 6 electroluminescence emission peaks at 465 nm were employed. The actual illumination optical
- 7 powers were calibrated by a Thorlabs 120 UV power sensors before the measurement.
- 8 Additionally, circularly polarized illumination (1 mW cm⁻²) was generated from an LED lamp
- 9 through a linear polarizer and quarter-wave plate (Nikon).
- 10 Transfer characteristics under illumination were recorded using the experimental sequence of
- dark, matched circularly polarized light, mismatched circularly polarized light, and then dark.
- In order to investigate the performance of OPTs, photoresponsivity (R) and photoswitching
- ratio (P) were calculated from transfer curves coupled with light illumination. The R and P
- values are typically defined by the following equation,

$$R = \frac{I_{ph}}{P_{inc}} = \frac{I_{light} - I_{dark}}{P_{inc}},$$

$$P = \frac{I_{light} - I_{dark}}{I_{dark}},$$

- where I_{ph} is the photocurrent, P_{inc} the incident illumination power, I_{light} the drain current under
- illumination, and I_{dark} the drain current in the dark condition.
- 19 *UV-Vis Spectroscopy and CD Spectroscopy:* The UV-vis spectra of solution and film states
- were measured using a Shimadzu UV-3600. The pristine PA-PTCDI and PA-PTCDI/DNA

- 1 blend films were deposited onto the glass substrates. Additionally, the CD spectra of solution
- 2 and films were collected using an Applied Photophysics Chirascan plus.
- 3 **Polarized Optical Microscopy (POM):** The optical textures of the films were obtained by POM
- 4 (LV100POL, Nikon, Tokyo, Japan) with a rotatable polarizer and analyzer and first-retardation
- 5 plate.
- 6 Atomic Force Microscopy: The AFM images of PDI and DNA-PDI films were measured using
- 7 the tapping mode with an SiN tip having a cantilever length of 115 μm and a resonant frequency
- 8 of ~400 kHz (Bruker, Multimode-8) an ICON Dimension microscope (Bruker) operated in a
- 9 "light" tapping mode in the air. 60 The scan rate was in the range of 0.5–1.0 Hz, and the
- resolution of AFM images was either 512 × 512 or 1024 × 1024 pixels. AFM probes
- 11 (MikroMasch, HQ:XSC11/AL BS) were used with a tip radius of 8 nm and spring constant of
- 12 1.5–2.2 N m⁻¹. AFM images were analyzed using Bruker Nanoscope Analysis 2.0 software.
- 13 Surface aggregates Orientation: The software (GTFiber) compiles and reproduces the DNA-
- 14 PDI aggregates in the AFM images by a backbone of single-pixel width, and each of them was
- 15 labeled with an orientation value from 0 to 180° for analytical results of the orientation maps
- in the insets of AFM images. The dispersion of the two-dimensional (2D) orientation
- distribution corresponded to the orientational order parameter S_{2D} , referred to as Herman's
- Orientation Factor. 61,62 Theoretically, S_{2D} is defined as

$$S_{2D} = 2\langle \cos^2 \theta_n \rangle - 1$$

- where θ_n is the angle between an individual fiber of each pixels and the AFM image's overall
- director, \vec{n} , which is selected as the average orientation of the population. Within the analysis,
- 22 S_{2D} represents between 0 and 1; the expected value of $\cos^2 \theta$ for a population of random
- angles θ is 0.5, yielding an S_{2D} of 0 invariant to the selection of the director, and a perfectly

- ordered population generated an $\langle \cos^2 \theta_n \rangle$ of 1, yielding an S_{2D} of 1. The average aggregates
- 2 director was plotted in each orientation distribution as a centered black line segment.⁴³

1 Figures

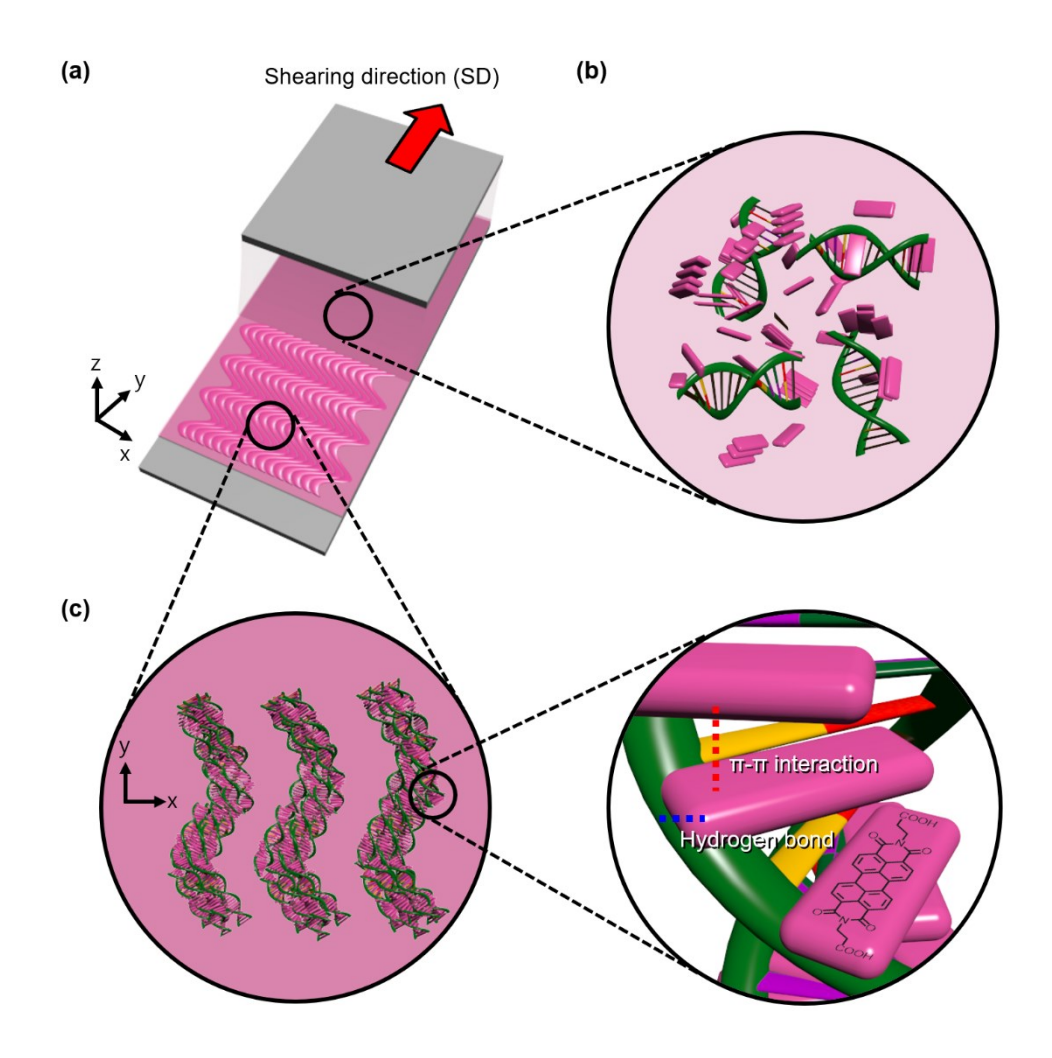
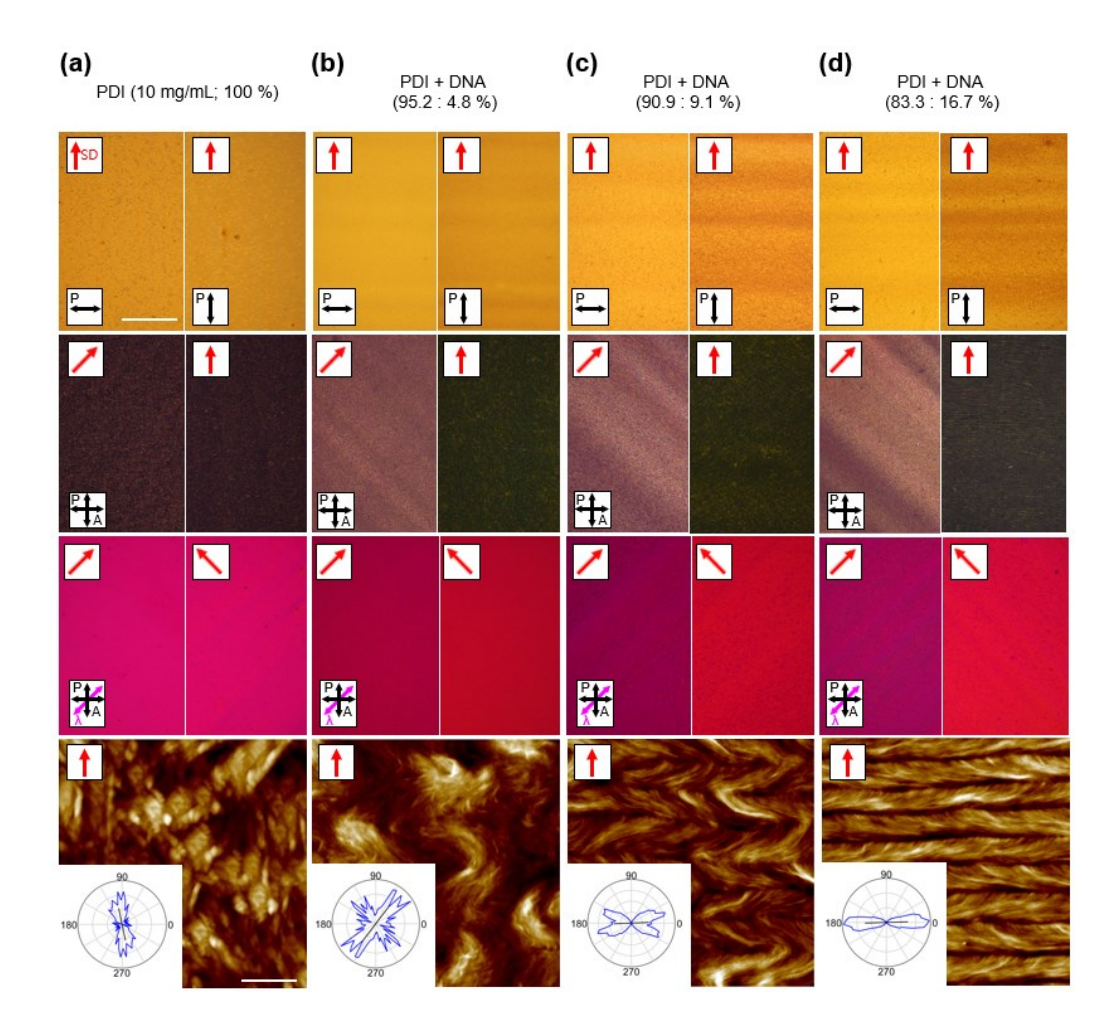


Figure 1. Schematic illustration of evaporation-induced self-assembled DNA- PA-PTCDI

- 4 **complex.** (a) Thin-film fabrication by solution shearing process. Molecular configuration of
- 5 randomly oriented (b) solution and resultant zigzag-like oriented (c) thin film state by solution
- 6 shearing (inset: chemical interaction and suggested conformation between PA-PTCDI and
- 7 DNA).

2



2 Figure 2. POM images and AFM topographic images of the sheared DNA-PDI complex

- 3 **films in each condition** (a) PDI (10 mg/ mL; 100 %), (b) PDI (95.2 %) + DNA (4.8 %), (c)
- 4 PDI (90.9 %) + DNA (9.1 %), and (d) PDI (83.3 %) + DNA (16.7 %). The scale bars in the OM
- 5 and AFM images are 100 μm and 1 μm, respectively. (inset: the radial axis and a diametrical
- 6 black line segment indicate the count of pixels of a given orientation the average orientation,
- 7 respectively, see Methods).

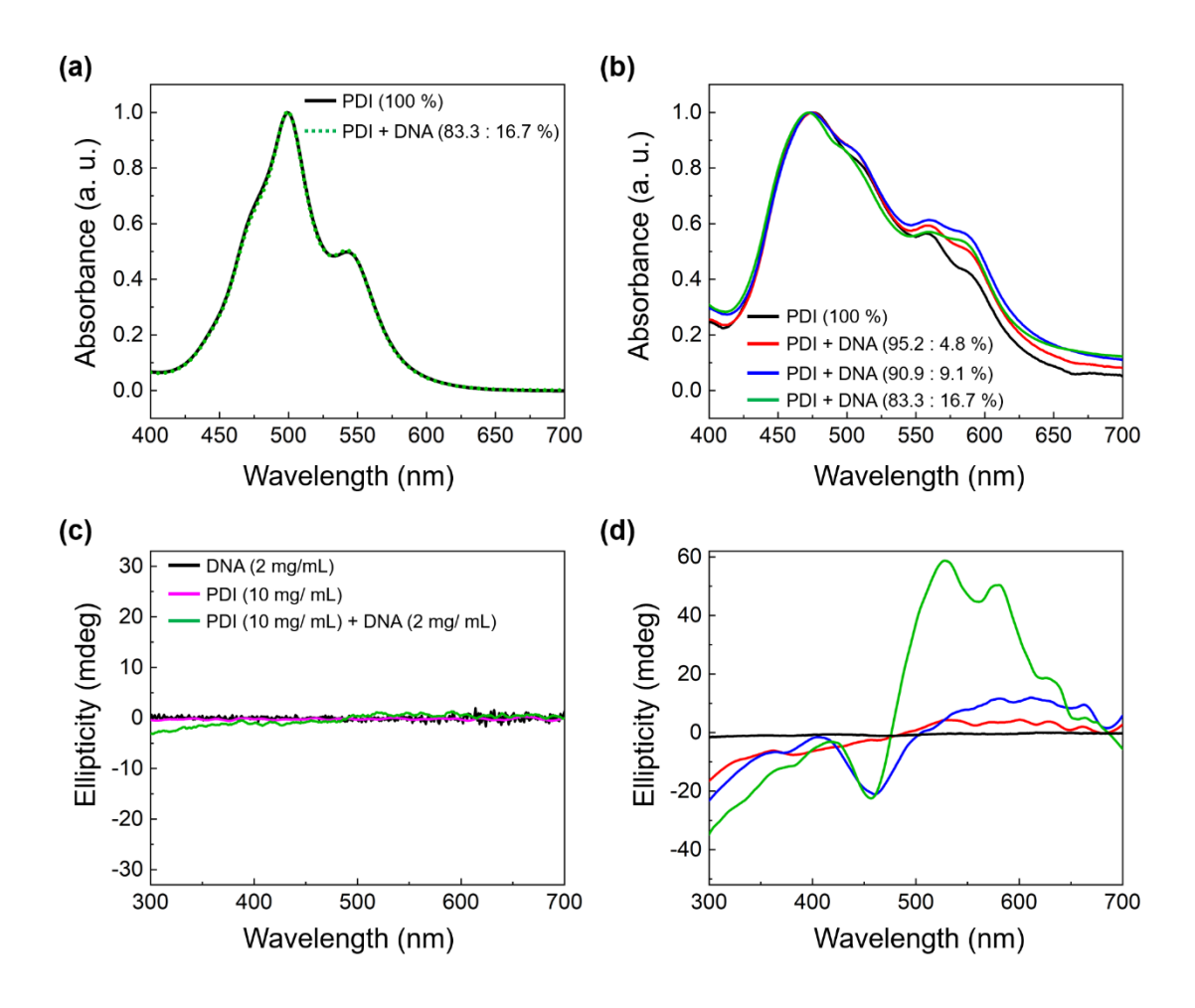


Figure 3. Optical properties of DNA-PDI solution and their shear aligned condensed films.

- 4 (a) UV-vis spectra of PDI (10 mg/ mL; 100 %) and PDI + DNA (83.3 : 16.7 %) in solution. (b)
- 5 UV-vis spectra of PDI and PDI + DNA blends with different DNA concentrations, such as
- 6 100 %, 95.2:4.8 %, 90.9:9.1 %, and 83.3:16.7 %. (c) CD spectra of solution state of DNA
- 7 (2 mg/ mL), PDI (100 %), and PDI + DNA (83.3 : 16.7 %). (d) CD spectra of PDI and PDI + $\,$
- 8 DNA blends with different DNA concentrations (100 %, 95.2:4.8 %, 90.9:9.1 %, and 83.3:
- 9 16.7 %).

2

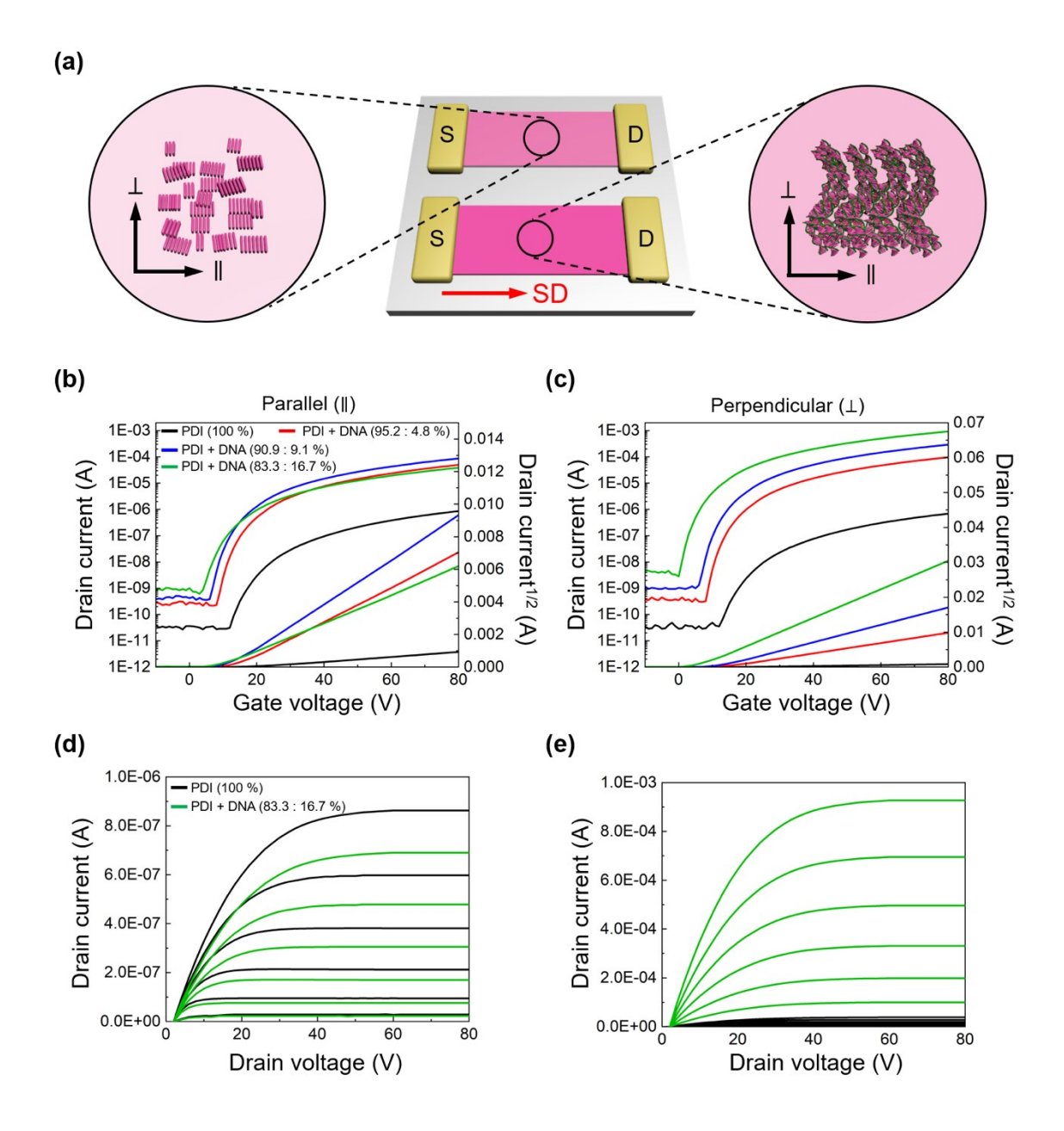


Figure 4. Opto-electrical characterization under different DNA concentrations. (a) Schematic illustration of OTFTs based on PDI without DNA and with DNA (inset: parallel (||) and perpendicular (\pm\)) direction to the shearing direction). Transfer characteristics of the sheared films of DNA-PDI blends when the source (S) / drain (D) channel direction was (a) parallel and (b) perpendicular to the shear direction. Representative output characteristics of the sheared film based on PDI (100 %) and PDI + DNA (83.3: 16.7 %) concentration in case

- of (c) parallel and (d) perpendicular case. The V_G range was from (d) 20 to 80 V with 10 V
- 2 steps.

Sample composition, PDI-DNA %		Mobility (cm ² V ⁻¹ s ⁻¹)	I _{ON} /I _{OFF}	V _{th} (V)
PDI (10 mg/ mL; 100 %)	II	$(3.9 \pm 1.2) \times 10^{-3}$	~ 104	15 ± 3.5
	Т	$(3.0 \pm 0.9) \times 10^{-3}$	~ 104	13 ± 3.2
PDI + DNA (95.2 : 4.8 %)	II	$(2.1 \pm 0.5) \times 10^{-1}$	~ 105	6 ± 2.3
	Т	$(4.1 \pm 1.2) \times 10^{-1}$	~ 105	8 ± 2.5
PDI + DNA (90.9 : 9.1 %)	II	$(3.7 \pm 1.1) \times 10^{-1}$	~ 105	5 ± 2.7
	Т	$(1.2 \pm 0.1) \times 10^{0}$	~ 105	5 ± 2.6
PDI + DNA (83.3 : 16.7 %)		$(1.6 \pm 0.5) \times 10^{-1}$	~ 104	4 ± 2.2
	Т	$(4.0 \pm 1.2) \times 10^{0}$	~ 105	0 ± 2.8

Table 1. BOFET performance of sheared DNA-PDI films at different DNA concentrations. Standard deviation is obtained from the 10 devices.

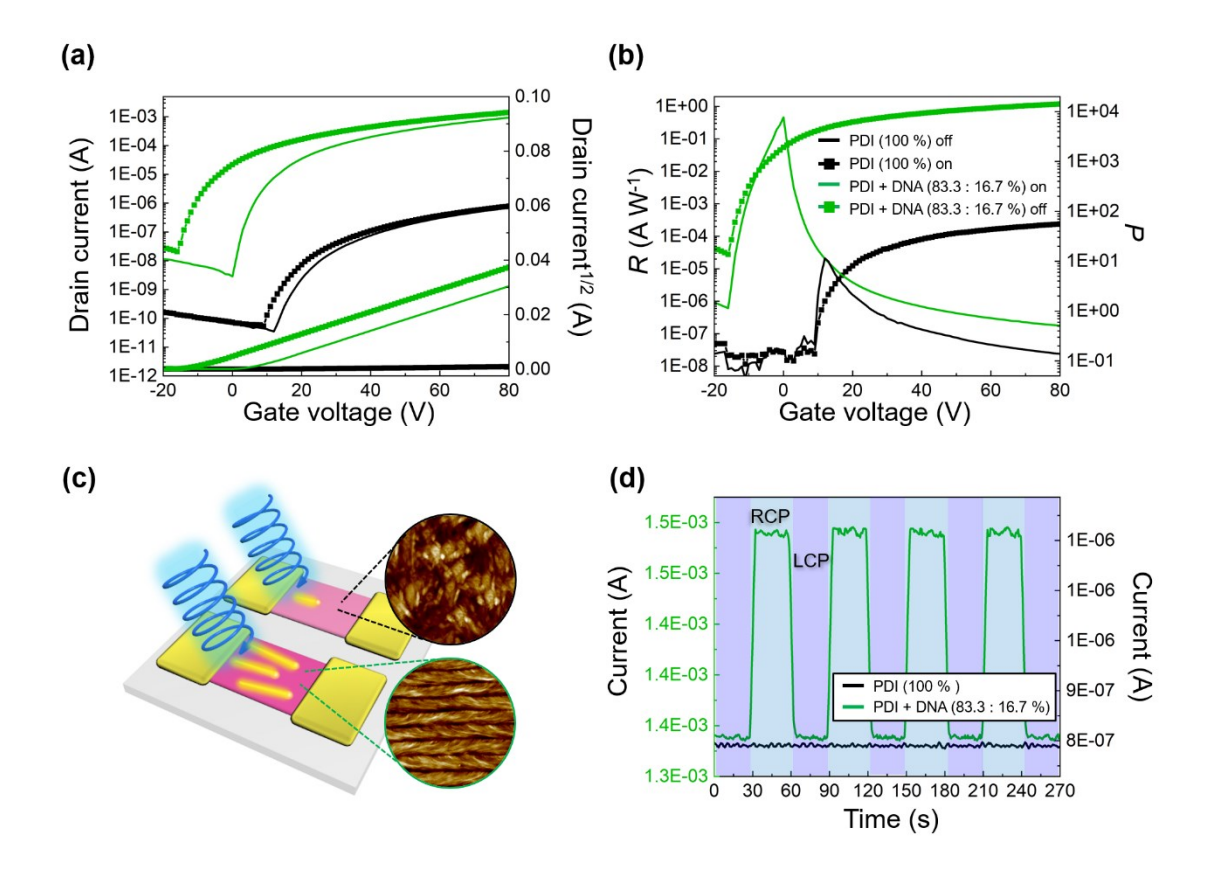


Figure 5. Chiro-electrical behavior of BOFETs. (a) I_{DS} – V_{GS} characteristics of PDI and PDI blended with DNA thin films in the dark and under monochromatic light illumination ($\lambda = 465$ nm) and vacuum conditions ($V_{DS} = 80$ V) with (b) Photoresponsivity and photoswitching ratio. (c) Schematic illustration of CPL-responsive DNA-PDI complex. (d) Real-time current signal of PDI and DNA-PDI complex under CPL illumination ($\lambda = 465$ nm).

1 References

- 3 1. Huang, J. et al. Printable and Flexible Phototransistors Based on Blend of Organic
- 4 Semiconductor and Biopolymer. Adv. Funct. Mater. 27, 1604163 (2017).
- 5 2. Myny, K. et al. Organic RFID transponder chip with data rate compatible with electronic
- 6 product coding. *Organic Electronics* **11**, 1176–1179 (2010).
- 7 3. Cho, J. H. et al. Printable ion-gel gate dielectrics for low-voltage polymer thin-film
- 8 transistors on plastic. *Nature Mater* 7, 900–906 (2008).
- 9 4. Henson, Z. B., Müllen, K. & Bazan, G. C. Design strategies for organic semiconductors
- beyond the molecular formula. *Nature Chem* **4**, 699–704 (2012).
- 5. Garnier, F. et al. Molecular engineering of organic semiconductors: design of self-assembly
- properties in conjugated thiophene oligomers. J. Am. Chem. Soc. 115, 8716–8721 (1993).
- 6. Yu, P., Zhen, Y., Dong, H. & Hu, W. Crystal Engineering of Organic Optoelectronic
- 14 Materials. *Chem* **5**, 2814–2853 (2019).
- 7. Ji, W. et al. Tunable Mechanical and Optoelectronic Properties of Organic Cocrystals by
- 16 Unexpected Stacking Transformation from H- to J- and X-Aggregation. ACS Nano 14, 10704—
- 17 10715 (2020).
- 18 8. Yuan, Y. et al. Ultra-high mobility transparent organic thin film transistors grown by an off-
- centre spin-coating method. *Nat Commun* **5**, 3005 (2014).
- 20 9. Bucella, S. G. et al. Macroscopic and high-throughput printing of aligned nanostructured
- 21 polymer semiconductors for MHz large-area electronics. *Nat Commun* **6**, 8394 (2015).
- 22 10. Nagamatsu, S. et al. Backbone Arrangement in "Friction-Transferred" Regioregular
- Poly(3-alkylthiophene)s. *Macromolecules* **36**, 5252–5257 (2003).

- 1 11. Han, M. J. et al. Highly Oriented Liquid Crystal Semiconductor for Organic Field-Effect
- 2 Transistors. ACS Cent. Sci. 4, 1495–1502 (2018).
- 3 12. Lin, F.-J. et al. Directional Solution Coating by the Chinese Brush: A Facile Approach to
- 4 Improving Molecular Alignment for High-Performance Polymer TFTs. Adv. Mater. 29,
- 5 1606987 (2017).
- 6 13. Sokolov, A. N. et al. From computational discovery to experimental characterization of a
- 7 high hole mobility organic crystal. *Nat Commun* **2**, 437 (2011).
- 8 14. Takimiya, K., Shinamura, S., Osaka, I. & Miyazaki, E. Thienoacene-Based Organic
- 9 Semiconductors. *Adv. Mater.* **23**, 4347–4370 (2011).
- 10 15. Brédas, J.-L., Beljonne, D., Coropceanu, V. & Cornil, J. Charge-Transfer and Energy-
- 11 Transfer Processes in π -Conjugated Oligomers and Polymers: A Molecular Picture. Chem. Rev.
- 12 **104**, 4971–5004 (2004).
- 13 16. Minemawari, H. et al. Inkjet printing of single-crystal films. Nature 475, 364–367 (2011).
- 14 17. Giri, G. et al. Tuning charge transport in solution-sheared organic semiconductors using
- 15 lattice strain. *Nature* **480**, 504–508 (2011).
- 18. Diao, Y. et al. Solution coating of large-area organic semiconductor thin films with aligned
- single-crystalline domains. *Nature Mater* **12**, 665–671 (2013).
- 18 19. Smith, J. et al. Solution-Processed Small Molecule-Polymer Blend Organic Thin-Film
- 19 Transistors with Hole Mobility Greater than 5 cm²/Vs. Adv. Mater. **24**, 2441–2446 (2012).
- 20 20. Kline, R. J. et al. Dependence of Regioregular Poly(3-hexylthiophene) Film Morphology
- 21 and Field-Effect Mobility on Molecular Weight. *Macromolecules* **38**, 3312–3319 (2005).
- 21. Vladimirov, I., Kühn, M., Geßner, T., May, F. & Weitz, R. T. Energy barriers at grain
- boundaries dominate charge carrier transport in an electron-conductive organic semiconductor.
- 24 *Sci Rep* **8**, 14868 (2018).

- 1 22. Diao, Y., Shaw, L. & Mannsfeld, S. C. B. Morphology control strategies for solution-
- 2 processed organic semiconductor thin films. *Environmental Science* 15 (2014).
- 3 23. Janneck, R., Vercesi, F., Heremans, P., Genoe, J. & Rolin, C. Predictive Model for the
- 4 Meniscus-Guided Coating of High-Quality Organic Single-Crystalline Thin Films. *Adv. Mater.*
- 5 **28**, 8007–8013 (2016).
- 6 24. Tremel, K. et al. Charge Transport Anisotropy in Highly Oriented Thin Films of the
- 7 Acceptor Polymer P(NDI2OD-T2). Adv. Energy Mater. 4, 1301659 (2014).
- 8 25. Biniek, L., Leclerc, N., Heiser, T., Bechara, R. & Brinkmann, M. Large Scale Alignment
- 9 and Charge Transport Anisotropy of pBTTT Films Oriented by High Temperature Rubbing.
- 10 *Macromolecules* **46**, 4014–4023 (2013).
- 11 26. Park, K. S. et al. Tuning conformation, assembly, and charge transport properties of
- 12 conjugated polymers by printing flow. Sci. Adv. 5, eaaw7757 (2019).
- 27. Park, S. M. et al. Fabrication of Chiral M13 Bacteriophage Film by Evaporation-Induced
- 14 Self-Assembly. *Small* **17**, 2008097 (2021).
- 15 28. Han, M. J. et al. Orientation Control of Semiconducting Polymers Using Microchannel
- 16 Molds. ACS Nano 14, 12951–12961 (2020).
- 17 29. Cha, Y. J., Park, S. M., You, R., Kim, H. & Yoon, D. K. Microstructure arrays of DNA
- using topographic control. *Nat Commun* **10**, 2512 (2019).
- 19 30. Cha, Y. J. et al. Orthogonal Liquid Crystal Alignment Layer: Templating Speed-Dependent
- 20 Orientation of Chromonic Liquid Crystals. ACS Appl. Mater. Interfaces 9, 18355–18361
- 21 (2017).
- 22 31. Cheng, Z. et al. Plasmonic-Enhanced Cholesteric Films: Coassembling Anisotropic Gold
- Nanorods with Cellulose Nanocrystals. *Advanced Optical Materials* 7, 1801816 (2019).
- 24 32. Nemati, A. et al. Chirality amplification by desymmetrization of chiral ligand-capped
- 25 nanoparticles to nanorods quantified in soft condensed matter. *Nat Commun* **9**, 3908 (2018).

- 1 33. Jeon, S.-W., Kim, D.-Y., Araoka, F., Jeong, K.-U. & Choi, S.-W. Nanosegregated Chiral
- 2 Materials with Self-Assembled Hierarchical Mesophases: Effect of Thermotropic and
- 3 Photoinduced Polymorphism in Rodlike Molecules. *Chem. Eur. J.* **23**, 17794–17799 (2017).
- 4 34. Kim, B., Choi, H., Lee, J., Araoka, F. & Choi, S. Circularly Polarized Luminescence
- 5 Induced by Chiral Super Nanospaces. Adv. Funct. Mater. 29, 1903246 (2019).
- 6 35. Livolant, F. & Leforestier, A. Condensed phases of DNA: Structures and phase transitions.
- 7 *Progress in Polymer Science* **21**, 1115–1164 (1996).
- 8 36. Oh, J.-W. et al. Biomimetic virus-based colourimetric sensors. Nat Commun 5, 3043 (2014).
- 9 37. Majumdar, S. et al. Cyclodextrin Modulated Type I Collagen Self-Assembly to Engineer
- Biomimetic Cornea Implants. Adv. Funct. Mater. 28, 1804076 (2018).
- 11 38. Oh, D. X. et al. Chiral nematic self-assembly of minimally surface damaged chitin
- nanofibrils and its load bearing functions. *Sci Rep* **6**, 23245 (2016).
- 39. Smalyukh, I. I., Zribi, O. V., Butler, J. C., Lavrentovich, O. D. & Wong, G. C. L. Structure
- and Dynamics of Liquid Crystalline Pattern Formation in Drying Droplets of DNA. *Phys. Rev.*
- 15 *Lett.* **96**, 177801 (2006).
- 40. Schneider, T., Golovin, A., Lee, J. C. & Lavrentovich, O. D. Lyotropic chromonic liquid
- 17 crystals in aligned films for applications as polarizing coatings. *Journal of Information Display*
- 18 **5**, 27–38 (2004).
- 19 41. Datar, A., Balakrishnan, K. & Zang, L. One-dimensional self-assembly of a water soluble
- perylene diimide molecule by pH triggered hydrogelation. *Chem. Commun.* **49**, 6894 (2013).
- 21 42. Cha, Y. J. & Yoon, D. K. Control of Periodic Zigzag Structures of DNA by a Simple
- 22 Shearing Method. *Adv. Mater.* **29**, 1604247 (2017).
- 43. Persson, N. E., McBride, M. A., Grover, M. A. & Reichmanis, E. Automated Analysis of
- Orientational Order in Images of Fibrillar Materials. *Chem. Mater.* **29**, 3–14 (2017).

- 1 44. Charlet, E. & Grelet, E. Anisotropic light absorption, refractive indices, and orientational
- order parameter of unidirectionally aligned columnar liquid crystal films. Phys. Rev. E 78,
- 3 041707 (2008).
- 4 45. Oswald, P., Géminard, J. C., Lejcek, L. & Sallen, L. Nonlinear Analysis of Stripe Textures
- 5 in Hexagonal Lyotropic Mesophases. J. Phys. II France 6, 281–303 (1996).
- 6 46. Gennes, P. G. D. Polymeric liquid crystals: Frank elasticity and light scattering. *Mol. Cryst.*
- 7 *Lig. Cryst.* **34**, 177–182 (1976).
- 8 47. Ciferri A., Krigbaum W. R., Meyer R. B., Polymer Liquid Crystals, Academic Press, New
- 9 York (1982).
- 10 48. Deegan, R. D. et al. Capillary flow as the cause of ring stains from dried liquid drops.
- 11 *Nature* **389**, 827–829 (1997).
- 49. Robertazzi, A., Krull, F., Knapp, E.-W. & Gamez, P. Recent advances in anion-π
- interactions. CrystEngComm 13, 3293 (2011).
- 14 50. Shang, X. et al. Morphogenesis and Optoelectronic Properties of Supramolecular
- Assemblies of Chiral Perylene Diimides in a Binary Solvent System. *Sci Rep* 7, 5508 (2017).
- 16 51. Shang, X. et al. Supramolecular Nanostructures of Chiral Perylene Diimides with
- 17 Amplified Chirality for High-Performance Chiroptical Sensing. Adv. Mater. 7 (2017).
- 52. Schulz, M. *et al.* Giant intrinsic circular dichroism of prolinol-derived squaraine thin films.
- 19 *Nat Commun* **9**, 2413 (2018).
- 53. He, T., Zhang, X., Jia, J., Li, Y. & Tao, X. Three-Dimensional Charge Transport in Organic
- 21 Semiconductor Single Crystals. Adv. Mater. 24, 2171–2175 (2012).
- 54. Lee, J. Y., Roth, S. & Park, Y. W. Anisotropic field effect mobility in single crystal
- 23 pentacene. Appl. Phys. Lett. 88, 252106 (2006).
- 24 55. Zhang, Y. et al. DNA Interlayers Enhance Charge Injection in Organic Field-Effect
- 25 Transistors. Adv. Mater. 24, 4255–4260 (2012).

- 1 56. Shi, W., Yu, J., Huang, W. & Zheng, Y. Performance improvement of a pentacene organic
- 2 field-effect transistor through a DNA interlayer. J. Phys. D: Appl. Phys. 47, 205402 (2014).
- 3 57. Podzorov, V. & Gershenson, M. E. Photoinduced Charge Transfer across the Interface
- 4 between Organic Molecular Crystals and Polymers. *Phys. Rev. Lett.* **95**, 016602 (2005).
- 58. El Gemayel, M. *et al.* Tuning the Photoresponse in Organic Field-Effect Transistors. *J. Am.*
- 6 *Chem. Soc.* **134**, 2429–2433 (2012).
- 59. Samanta, S. K., Song, I., Yoo, J. H. & Oh, J. H. Organic n-Channel Transistors Based on
- 8 [1]Benzothieno[3,2- b]benzothiophene-Rylene Diimide Donor-Acceptor Conjugated
- 9 Polymers. ACS Appl. Mater. Interfaces **10**, 32444–32453 (2018).
- 10 60. McConney, M. E., Singamaneni, S. & Tsukruk, V. V. Probing Soft Matter with the Atomic
- 11 Force Microscopies: Imaging and Force Spectroscopy. *Polymer Reviews* **50**, 235–286 (2010).
- 12 61. Murphy, J. N., Harris, K. D. & Buriak, J. M. Automated Defect and Correlation Length
- Analysis of Block Copolymer Thin Film Nanopatterns. *PLoS ONE* **10**, e0133088 (2015).
- 14 62. Jordens, S., Isa, L., Usov, I. & Mezzenga, R. Non-equilibrium nature of two-dimensional
- isotropic and nematic coexistence in amyloid fibrils at liquid interfaces. *Nat Commun* **4**, 1917
- 16 (2013).